Planetary and Space Science xxx (2018) 1–11

Contents lists available at ScienceDirect

Planetary and Space Science

journal homepage: www.elsevier.com/locate/pss

Automated reconstruction of subsurface interfaces in Promethei Lingula near the Martian south pole by using SHARAD data

S. Xiong *, J.-P. Muller

Imaging Group, Mullard Space Science Laboratory, University College London, Department of Space and Climate Physics, Holmbury St. Mary, Surrey, RH5 6NT, UK

ARTICLE INFO

Keywords:
Martian south pole
Subsurface mapping
Radar stratigraphy
Promethei Lingula
SHARAD

ABSTRACT

Subsurface layers are preserved in polar regions on Mars, which are considered to be a record of past climate changes on Mars. Orbital radar instruments like the SHAllow RADar (SHARAD) on board Mars Reconnaissance Orbiter (MRO) transmit radar signals to Mars and receive a set of signals returned from interfaces having a contrast in dielectric properties in the probed subsurface regions. These subsurface layers which are preserved in the upper ≈ 1 km of the Martian Polar Layered Deposits (PLDs) can be observed in SHARAD radargrams. Extraction of these layering features is the preliminary work before interpreting and understanding their origins. In this study, we use a new method based on log-Gabor filtering and Continuous Wavelet Transform (CWT)-based peak detection to extract subsurface radar reflections and a workflow to remove clutter reflections in order to reconstruct 3-D subsurface layers. These methods and workflow are then tested on the SHARAD data in the Promethei Lingula region near the Martian south pole. The results show that following this workflow, the ground surface and six subsurface interfaces can be reconstructed, which aids in the interpretation of the depositional and erosional history of this region.

1. Introduction

Radar sounding techniques were proposed in the 1960s for investigating subsurface areas of glaciers on Earth. It is a non-intrusive and direct imaging technique to obtain subsurface information, which is different from surface imagery that only provides surface features from which one may be able to infer subsurface conditions. The radar sounders transmit waves to the probed regions and record the backscattered signals. For penetrating the surface, they usually work at low frequency (several megahertz to hundreds of megahertz). The resultant images acquired by using the radar sounders are called radargrams, in which the x-axis represents the geographical locations of the profiles and the y-axis is the two-way travel (TWT) time. Therefore, a radargram shows a sounding profile taken along a certain ground track. Each of the TWT time signals (each column in a radargram) represents a series of radar reflections, which may indicate changes in the dielectric boundaries underground.

One important application of the radar sounding data is subsurface investigations of icy regions, such as Greenland, Antarctica and Martian poles. Subsurface layers extending within the icy regions provide clues for inferring depositions and erosions of atmospheric precipitation materials, such as snow on Earth and CO_2 frost or H_2O snow and atmospheric dust on Mars. Studying the stratigraphy of ice sheets allows building up a relationship between ice age and depths. It reveals ice mass balance in the past and provides important information to constrain ice flow models (Vaughan et al., 1999; Waddington et al., 2007). Studying the stratigraphy of PLDs deepens the understanding of their formation and relevant past climate changes. Subsurface layers in the upper 1 km of the Martian PLDs have been imaged by SHAllow RADar (SHARAD) on board the NASA Mars Reconnaissance Orbiter (MRO) at a vertical resolution of about 15 m using the dielectric constant of free space (Seu et al., 2004, 2007; Flamini et al., 2007). The spatial resolution of the radargrams is approximately 450 m × 3 km (along track by across track). The range sampling is 37.5 ns as two-way travel time, corresponding to 5.63 m in free space and slightly more than 3 m in an icy subsurface (assuming a dielectric constant of 3.4). It is noteworthy that this represents nearly a factor of three in oversampling of the inherent range resolution of 15 m. The SHARAD instrument has been orbiting Mars since 2006 and covers 36.1% of the Martian surface (Global coverage can be seen at https://sharad.psi.edu/maps/). There is a dense data coverage in the polar regions due to the polar orbit. Extraction and analysis of subsurface layers from these data has recently expanded from traditional

* Corresponding author.
E-mail addresses: siting.xiong.14@ucl.ac.uk (S. Xiong), j.muller@ucl.ac.uk (J.-P. Muller).

https://doi.org/10.1016/j.pss.2018.08.001
Received 10 March 2018; Received in revised form 2 August 2018; Accepted 4 August 2018
Available online xxxx

manual investigations to the use of 3-D imaged volumes (Foss et al., 2017). These semi-automated or automated, 2-D or 3-D methods allow the extraction of relevant information from these data in a more and more rapid and effective manner, thus facilitating the study of subsurface features in relation with the geological and climate history.

The development of automated techniques to extract subsurface layers from radargrams has not been addressed sufficiently in the literature. Related studies mainly contribute to the automated analyses of data acquired by Ground Penetrating Radars (GPRs) showing linear and hyperbolic returns (Capineri et al., 1998; Delbo et al., 2000; Gamba and Lossani, 2000; Al-Nuaimy et al., 2001; Pasolli et al., 2009). Few attempts have been reported in the literature to address the automated detection of subsurface linear features from Martian radar sounding data. Freeman et al. used a combination of filters followed by a thresholding operation to extract subsurface layers from the SHARAD radargrams but this method does not address the task of labelling layers which are formed in different ages (Freeman et al., 2010). Ferro et al. proposed an automated method to extract subsurface layers from radar sounder data acquired in Martian icy regions (Ferro and Bruzzone, 2013). In their work, a BM3D filter (Dabov et al., 2007) was followed by a Steger filter (Steger, 1996) and used to extract lines from radargrams.

As observed in the SHARAD radargrams, the subsurface layers preserved in the Martian PLDs share a similarity with fingerprints. Since log-Gabor filtering has been widely applied to enhance images of fingerprints, it is likely that this filtering method might also work with the SHARAD radargrams, although there is no record of any literature reporting its application to this field. Furthermore, considering the SHARAD radargrams only show a 2-D profile of the probed region, it is necessary to combine radargrams from multiple orbits to reconstruct a 3-D subsurface structure. Foss et al. (2017) first demonstrated the retrieval of 3-D volumes for both polar regions of Mars. Their 3-D volume imaging is built from 2-D interpolated images at every time delay position. The 3-D volumes of SHARAD data are available at https://sharad.psi.edu/3D/.

In this paper, we propose an automated method based on the combination of a log-Gabor filtering and a Continuous Wavelet Transform (CWT) to extract the subsurface reflections from SHARAD radargrams. Clutter reflections are simulated and removed from these subsurface reflections, which are subsequently partitioned into different layers in the 3-D domain by using classification methods. The proposed workflow for reconstructing the 3-D subsurface layers is introduced in Section 3. To test the proposed method and workflow, we choose a study area located in the Promethei Lingula (PL) region over the Martian south pole. In this region, the subsurface layers extend laterally to hundreds of kilometres, and at least one angular unconformity is revealed. The 2-D and the following 3-D processing are tested on SHARAD radargrams covering the study site, which are introduced in Section 2. The experimental results are demonstrated and discussed in Sections 4 and 5.

2. Study site and data

The Promethei Lingula is a low-relief plateau at the margin of the SPLD, as shown in Fig. 1. Together with Ultimi Lobe (UL), it is dissected and separated by three reentrant canyons, namely Promethei Chasma (PC), Ultimum Chasma (UC) and Chasma Australe (CA) (Byrne and Ivanov, 2004). The Promethei and Ultimum Chasma have rugged floors exposing Hesperian and Noachian materials. A similarly oriented but shallower canyon, Australe Sulci, features dense, parallel sets of curvilinear grooves, canyon-transecting sinuous ridges and circular and elongated mounds (Kolb and Tanaka, 2006). Three sequences of layered deposits have been identified in this region. Between the top and the second layer sequences, an angular unconformity has been revealed by analysing high-resolution surface images (Kolb and Tanaka, 2006) and from analysing manually SHARAD radargrams (Seu et al., 2007; Milkovich et al., 2009; Guallini et al., 2018). Although layer exposures can be found extending the South Polar Layered Deposits (SPLD) in the surface images, such as from Mars Orbital Camera (MOC) and Thermal Emission Imaging System (THEMIS) images, the extent of these layer sequences is observed to be interrupted in the SHARAD radargrams. In SHARAD radargrams, the subsurface layer sequences are only revealed to be continuous within the Promethei Lingula region. Guallini et al. postulated that the oscillations in Martian axial obliquity could have controlled local climate conditions in the past, leading to the current geological records according to their analyses of the geologic units in the region (Guallini et al., 2018).

The study site is selected within the Promethei Lingula as the white rectangle shown in Fig. 1, within which the elevation of the angular unconformity has been interpolated from manual delineation on

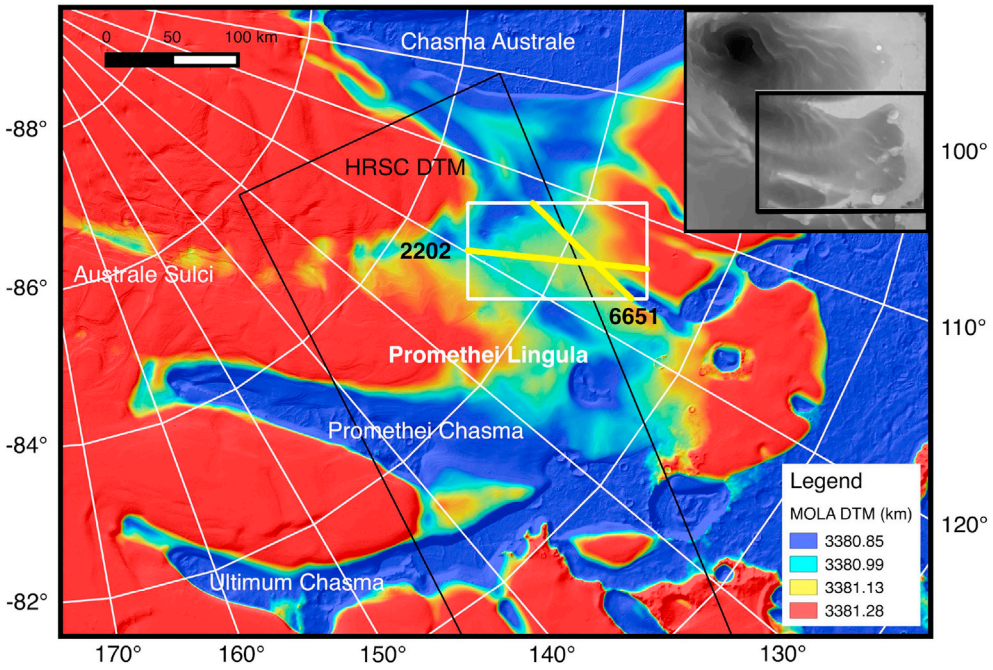

Fig. 1. The coverage of the study site is denoted by the white rectangle in the Promethei Lingula (PL) region, under which is the Mars Orbiter Laser Altimeter (MOLA) DTM (MEGDR at 512 pixels/degree or ≈115 m/pixel, the elevation is here referred to the Martian centre of mass). The black polygon indicates a scene of HRSC DTM (Product id is h2165). The yellow lines show the footprints within the PL region of the SHARAD radargrams from orbits 2202 and 6651. (For interpretation of the references to colour in this figure legend, the reader is referred to the Web version of this article.)

SHARAD radargrams by Guallini et al. (2018). In this study, 146 SHARAD radargrams are used. In addition, a High Resolution Stereo Camera (HRSC) Digital Terrain Model (DTM) (product id: h2165) covering a large part of this region is created and used for simulating the clutter reflections. The HRSC DTM was produced using the methods developed by Kim and Muller (2009) who use the open source VICAR programme together with photogrammetry software from DLR (Deutschen Zentrums fr Luft-und Raumfahrt) with image matching based on the GOTCHA (Gruen-Otto-Chau) algorithm (Putri et al., under review).

3. Methods

In this study, a 3-D reconstruction of subsurface layers is obtained by using the SHARAD radargrams in four steps, the first three of which are carried out in the 2-D raster domain on the radargrams. Firstly, the original radargram is enhanced by applying a log-Gabor filtering which improves the contrast of the angular linear features. Secondly, a CWT-based peak detection method is applied to the filtered radargram to extract the subsurface reflections. Thirdly, an external DTM is used to simulate the clutter reflections which are then compared to the subsurface reflections to eliminate any false detections. Finally, after the detection of subsurface reflections from all radargrams located within the study area, the 3-D coordinates of the extracted reflection positions are treated as a point cloud, to which clustering methods are applied to distinguish the subsurface layers. The overall processing flow is shown in Fig. 2.

3.1. Radargram enhancement

The SHARAD radargrams usually show low Signal to Noise Ratio (SNR), which is probably related to the low transmitted power (10 W) of SHARAD. Therefore, an image enhancement is beneficial to suppress the noise and to improve the contrast of linear features. Image denoising methods, include such techniques as the Block-Matching and 3D (BM3D) (Papari and Petkov, 2011), Bilateral filtering (Tomasi and Manduchi, 1998), wavelet shrinkage denoising (Chen and Qian, 2011) etc. Among these methods, the log-Gabor filtering was found to be most effective in enhancing the contrast of the linear features.

The denoising method using log-Gabor functions was proposed by (Kovesi, 1999), as shown in Equation (1). This enables one to calculate the amplitude and phase of the input image for a given frequency, f and orientation, θ, of the filtering kernels. f_0 and θ_0 are the central frequency and orientation of the filtering kernels. σ_f and σ_θ are the bandwidth parameter and width parameter of the orientation, which are usually set to be constant to maintain the same shape of the filter while adjusting the frequency and orientation. To extract angular features at different directions and frequencies, a set of radial filters and a set of angular filters are combined. For example, f and θ are chosen exhaustively from the $f \in (f_1, f_2, \ldots, f_N)$ and $\theta \in (\theta_1, \theta_2, \ldots, \theta_N)$.

$$G(f,\theta) = exp\left(-\frac{(log(f/f_0))^2}{2(log(\sigma_f/f_0))^2}\right) exp\left(-\frac{(\theta-\theta_0)^2}{2\sigma_\theta^2}\right) \quad (1)$$

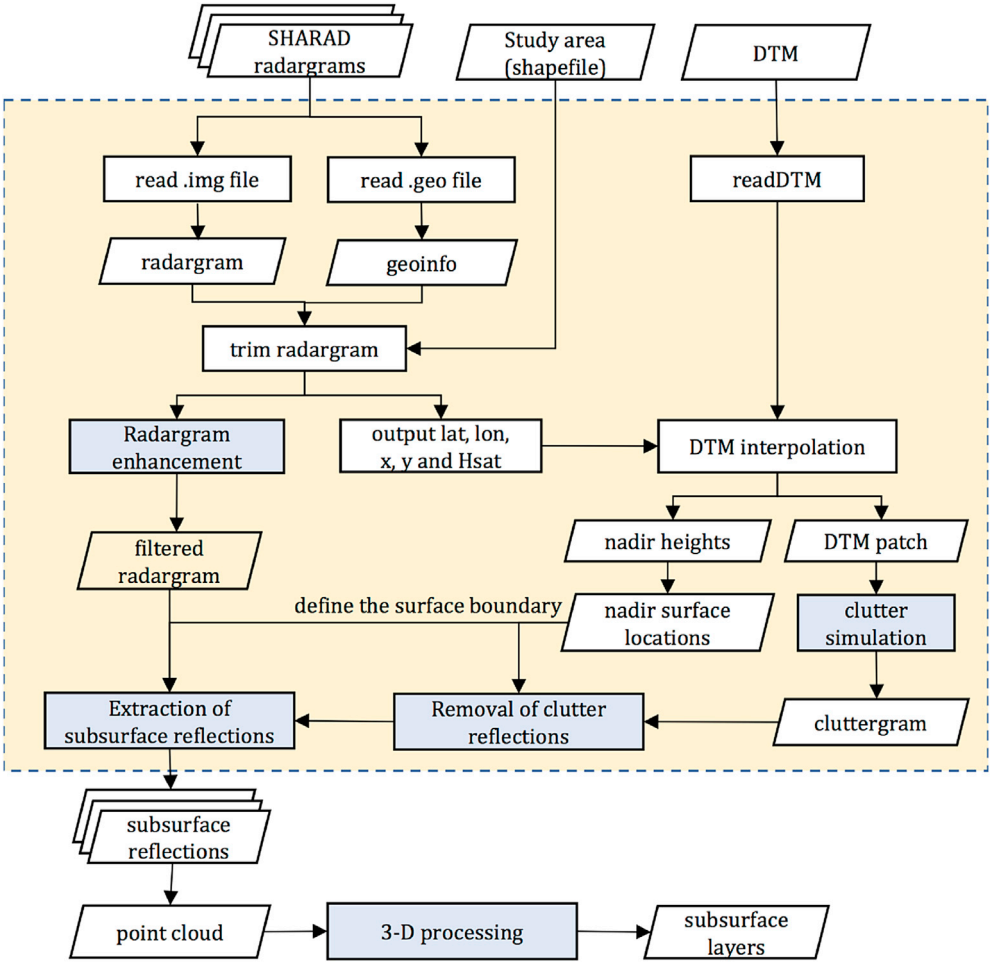

Fig. 2. The processing workflow for extracting subsurface layers and reconstructing their 3-D structures. The blue rectangles show the four primary steps and the yellow highlight with dashed borders is the 2-D raster processing applied to each SHARAD radargram. The Hsat is the height of satellite. (For interpretation of the references to colour in this figure legend, the reader is referred to the Web version of this article.)

The phase preserved denoising keeps the phase unchanged while shrinks the amplitude with a threshold, which is determined by using the Rayleigh distribution as it is when the signal is purely Gaussian white noise. A threshold, T, is determined from the amplitude response as expressed in Equation (2), where μ_r and σ_r describe the Rayleigh distribution of the filter response and k is typically in the range of 2–3. The μ_r and σ_r can be calculated from the standard deviation, σ_g, of the amplitude response as shown in Equation (3). A detailed description of the threshold determination is described in Kovesi (1999).

$$T = \mu_r + k\sigma_r \tag{2}$$

$$\mu_r = \sigma_g\sqrt{\frac{\pi}{2}}, \sigma_r = \sigma_g\sqrt{\frac{4-\pi}{2}} \tag{3}$$

3.2. Extraction of subsurface reflections

The radargram is a combination of a series of time signals at every footprint. In each column of the radargram, one dielectric boundary is recorded as one peak. Therefore, detecting linear features from radargrams can be resolved by detecting the peaks from each column in the enhanced radargram. The CWT-based peak detection can be used for detecting these peaks along each column in the radargrams (Du et al., 2006; Xiong et al., 2017). It is realised by applying the CWT to each column of the radargram, $x(t)$, to obtain the wavelet coefficients, $C(a,b)$, which are calculated using Equation (4). The a is the wavelet scale and b is the transitional value which is set to 1 in this case as the wavelet is moving along the column. Then a threshold is determined as the maximum value of the wavelet coefficient above surface reflections which can be detected using the method proposed by Mouginot et al. (2010). The peaks having a wavelet coefficient larger than this threshold are extracted as strong radar reflections.

$$C(a,b) = \frac{1}{\sqrt{a}}\int_{-\infty}^{\infty} x(t)\psi\left(\frac{t-b}{a}\right)dt \tag{4}$$

$$\psi_{mexh}(t) = \frac{2}{\sqrt{3}\pi^{1/4}}\left(1-t^2\right)e^{-t^2/2} \tag{5}$$

The Mexican hat (Ricker) wavelet (Torrence and Compo, 1998) as expressed in Equation (5) is used in this study. If several scales are applied to the CWT, a scalogram can be derived representing the wavelet response to all scales. At each scale, the peaks are detected by using the threshold obtained at this scale. The peaks detected over all scales are combined into the final detected peaks. The larger the scale is, the fewer but more reliable the peaks are detected.

3.3. Removal of clutter reflections

Due to the nadir-looking geometry of SHARAD and the large Field of View (FOV) of the radar beams, it is possible that reflections from features beyond the nadir point of the flight track arrive earlier at the receiver than the subsurface reflections at the nadir of the SHARAD. These interfering reflections come from off-nadir surface reflections or off-nadir subsurface reflections rather than the nadir subsurface reflections.

The off-nadir reflections are termed clutter reflections and can be simulated by using an external DTM. In this study, the simulation method proposed by Ferro and Bruzzone (2013) is used for simulating clutter reflections which can then be removed from extracted reflections from the filtered radargrams. This simple model described in Equation (6) considers no local information, such as local incidence angle and surface roughness.

$$\xi_S(i,t) = K\cdot\sum_{(x,y)\in A_{(i,t)}}\frac{[t-2R(x,y)]}{R(x,y)^4} \tag{6}$$

where $R(x,y)$ is the distance from the planar position (x,y) of a reflector in the cluttergram to the SHARAD antenna, i denotes the column number of the cluttergram and t denotes the time delay of reflection which can be converted to pixel coordinates by assuming a single dielectric constant. $A_{(i,t)}$ is the area in which every planar position (x,y) can be converted to the same position (i,t) in the cluttergram.

The SHARAD radargrams have been co-registered by US SHARAD team to the Mars Orbiter Laser Altimetry (MOLA) DTM. The elevations of the surface reflections should be the same as those from the MOLA DTM when there is no clutter reflection. However, when there are clutter reflections, the surface reflections in the radargrams may not be caused by the actual surface as measured in the MOLA DTM. During the simulation of the cluttergram by using the DTM, the locations of nadir surface reflections can be identified, which should have the shortest time delay compared with other nadir subsurface reflections. The identified nadir surface reflections can be transformed to image coordinates, thus delineated in the radargrams to limit the surface boundary.

The simulated radargram is here called a cluttergram. Foss et al. (2017) found the radargrams are misaligned with each other due to residual, along-track-variable delays introduced by the Martian ionosphere. Therefore, there may be a resultant slight offset between the surfaces of the radargram and cluttergram even when there are no occurrences of clutter reflections. However, the surface of the radargram should be congruent with the surface of cluttergram and the surface inverted from nadir elevations (nadir surface) if no off-nadir reflection arrives earlier than the nadir reflection. In this study, the surface of the radargram is detected and aligned with the surface of the cluttergram (detected in the same way as the radargram surface) when the offset is not too large (a threshold needs to be set for the allowed offset). Meanwhile, in each column of the cluttergram, a threshold (0.5 * value of surface return) is applied to pick up the suspected pixels as clutter reflections. Subsequently, the reflections in the radargrams are removed if they are near one suspected clutter reflection (below or above it to within 5 pixels). If the offset exceeds the threshold, then all the reflections along this column are regarded as clutter. After the removal of the clutter reflections, all remaining subsurface reflections are preserved. Their x-, y-coordinates, heights (that are referenced to the MOLA sphere radius of 3396 km) and radar amplitude are then output for further 3-D processing.

3.4. Three-dimensional(3-D) processing

The 3-D coordinates, namely geographical x and y coordinates and elevations, are extracted at all points which have been detected in the previous steps. Subsurface isochrones can then be generated by clustering all the points into several layer groups.

In this study, we use the Density-Based Spatial Clustering of Applications with Noise (DBSCAN) (Ester et al., 1996) to initially classify the points. The DBSCAN algorithm classifies data according to their density distribution. However, during the clustering, point groups with a small number of points can also be formed. Since the subsurface layers are generally distinguishable in the vertical direction, a hierarchical clustering is applied to agglomerate the pre-classified groups by the DBSCAN algorithm given a desired cluster number.

4. Results

4.1. The enhancement of SHARAD radargrams

The SHARAD radargram from orbit 2202, which is shown in Fig. 3(a), is here used to illustrate the results of the log-Gabor filtering. The traces from 3718 to 3896 of this radargram shown in white rectangle in Fig. 3(a) are used as test data since it contains extensive layered features. The log-Gabor filtering is applied to this subset radargram and the result is shown in Fig. 3(b), along with filtering results by BM3D (Fig. 3c) and Bilateral filtering (Fig. 3d). Fig. 3(e) shows one profile from column 3800

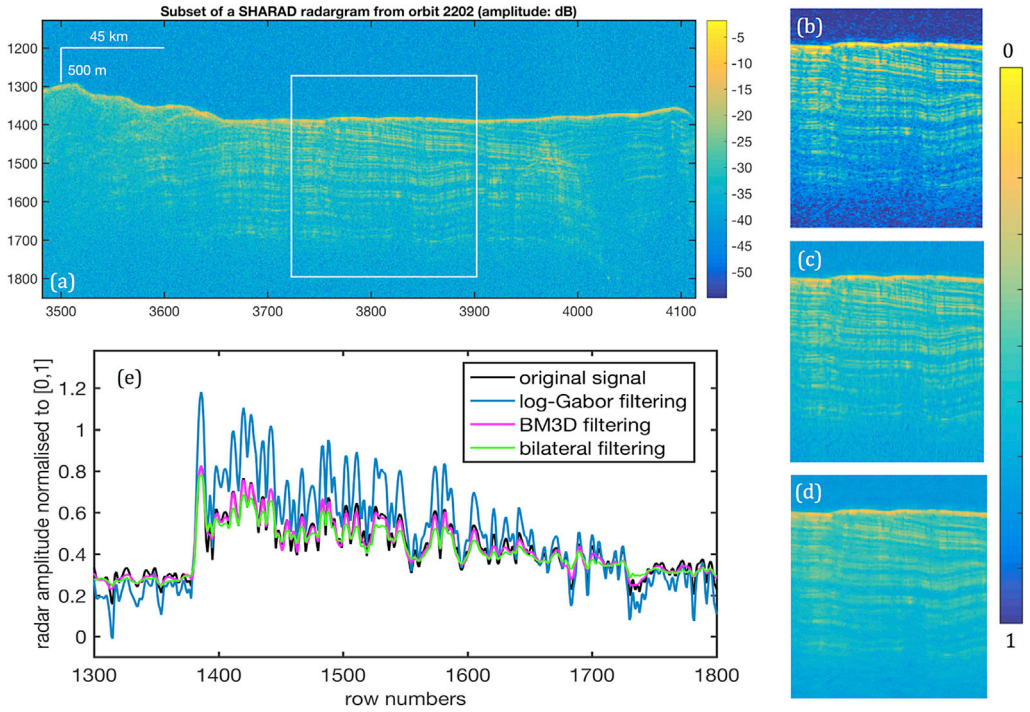

Fig. 3. (A) The subset of a SHARAD radargram from orbit 2202. The vertical scale bar of 500 m is the vertical range when using the dielectric constant of free space; the filtered radargrams after (b) log-Gabor filtering; (c) BM3D filtering; (d) Bilateral filtering; (e) column 3800 in the SHARAD radargram (orbit 2202).

of the unfiltered and filtered radargrams. The log-Gabor filtering performs the best in enhancing the contrast between the signals representing linear features and noise amongst the three methods.

In the log-Gabor filtering algorithm, two parameters, namely the number of frequencies and the multiplication frequency factor define the set of frequencies while the number of orientations defines the set of orientation angles, which are described in Section 3.1. The comparison of filtered radargrams resulting from different input parameters is shown in Fig. 4. The more frequency components are included, the less contrast the linear features have. The contrast of linear features relative to the background is reduced as their width becomes thinner when fewer frequency components are included, such as Fig. 4(b) and (e). The number of orientations has less effect on the filtered results, which is probably due to less curvature of individual layers. The signals along the column of 3800 (white lines in each subfigure of Fig. 4) of filtered radargrams are plotted. Signals above the surface return and lower down the radargrams vary around zero and the filtered signal follows the trend of the original one when the number of frequencies is 5 and the multiplication factor of the frequency is 3. To preserve the information of subsurface features as far as possible, the parameters of Fig. 4(b) are chosen as the input parameters for enhancing the radargrams. The parameters of Fig. 4(a) are the same as those for producing the Fig. 3(b).

4.2. *Clutter simulation and removal of clutter reflections*

Clutter reflections are simulated using an external DTM. Fig. 5 shows

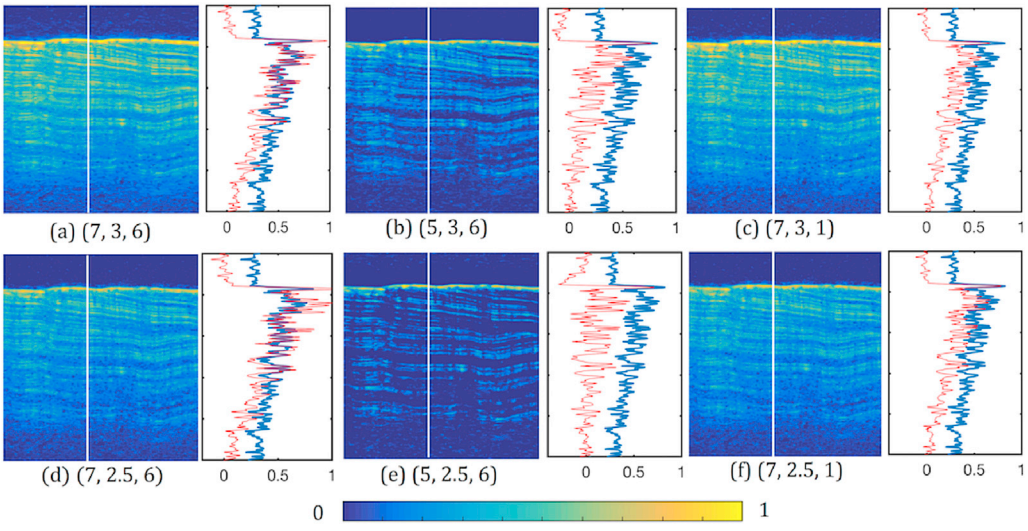

Fig. 4. (A-f) Comparison of different input parameters for log-Gabor filtering. The parameters in brackets are the number of frequencies, multiplication frequency factor and number of orientation angles. The signals along the column of 3800 of the filtered radargrams are demonstrated in the plots, the signals are radar amplitude normalized to [0,1].

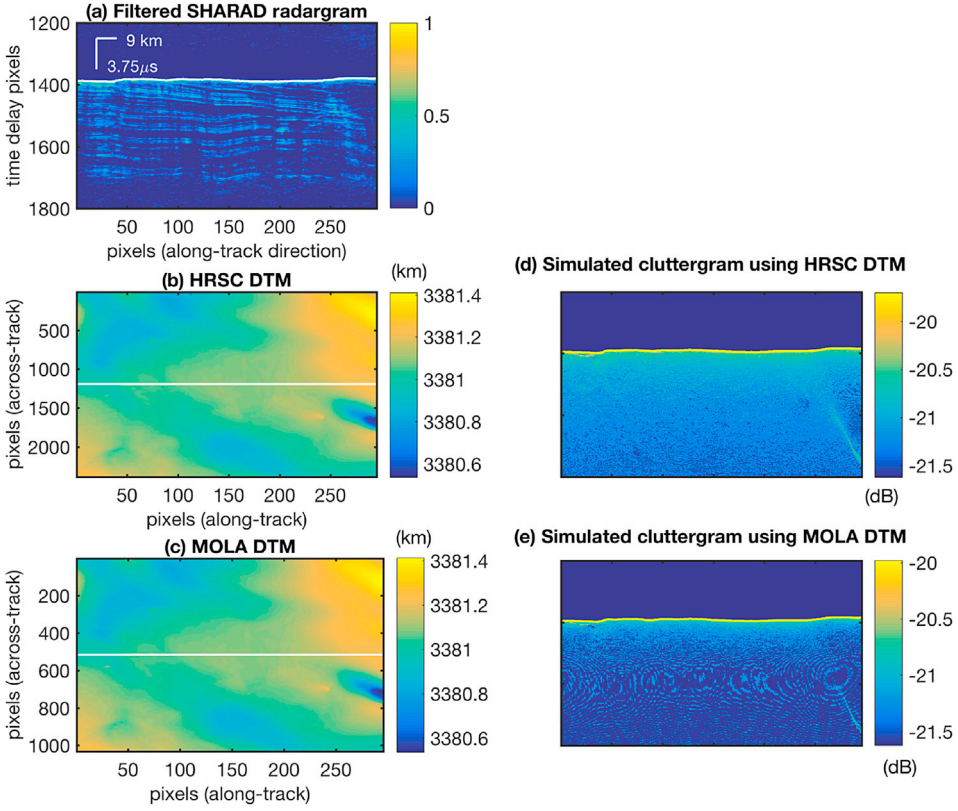

Fig. 5. Interpolated DTMs used to simulate cluttergrams for a subset (column 3718 to 4012) of SHARAD radargram from orbit 2202: (a) The filtered radargram; Interpolated (b) HRSC DTM and (c) MOLA DTM along the SHARAD track; Cluttergrams simulated using (d) HRSC and (e) MOLA DTM. The yellow lines in (d) and (e) show the locations inverted from surface DTM at nadir footprints. (For interpretation of the references to colour in this figure legend, the reader is referred to the Web version of this article.)

two cluttergrams which are simulated by HRSC and MOLA DTMs respectively for one part (from 3718 to 4012 columns) of the whole radargram from orbit 2202. The footprints of the partial radargram is shown in Fig. 1. The 50 m HRSC DTM has higher resolution than the corresponding MOLA DTM, which leads to a detailed simulated cluttergram shown in Fig. 5(d). Therefore, the HRSC DTM is selected as the external DTM to simulate the cluttergrams. In areas where there is no coverage of HRSC DTM, MOLA DTM is used for simulating the clutter reflection.

To investigate the relationship between the radargram and the cluttergram, a subset (rows from 1370 to 1470) of the SHARAD radargrams from orbit 2202 is studied in detail. Fig. 6(a) shows the filtered radargram from which an offset between the radargram surface (black line) and nadir surface (yellow line) can be observed. The signal along column

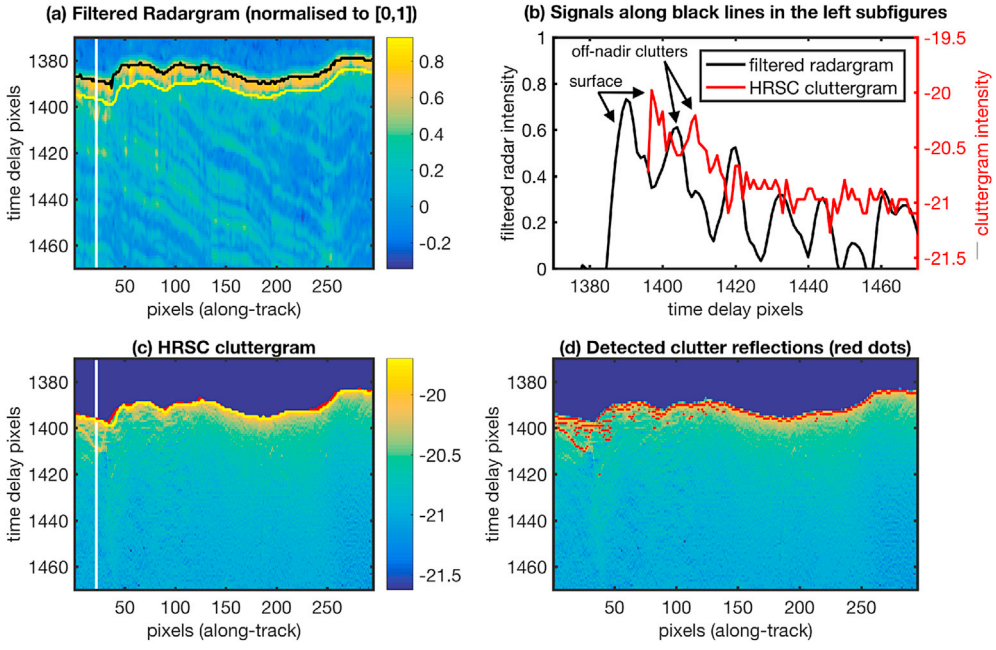

Fig. 6. (A) Surface reflections and surface of cluttergrams from the HRSC DTM; (b) Signals along column 22 of the filtered radargram and HRSC cluttergram; (c) HRSC cluttergram and (d) detected clutter reflections from the HRSC cluttergram.

22 (white vertical line in Fig. 6(a)) is shown in Fig. 6(b), the first high response represents the surface while the second one represents the clutter reflection which can be observed in both the radargram and cluttergram. Fig. 6(c) demonstrates detected cluttergram surface (red line) and the nadir surface (yellow line) on the HRSC cluttergram. Here we can also observe an offset between these two surfaces. Fig. 6(d) shows the detection of clutter reflections (including the surface returns) from the cluttergram, which can be later used for removing the clutter reflections from the detected subsurface reflections by aligning with the surface responses indicated by the black arrows shown in Fig. 6(b).

4.3. Extraction of subsurface reflections

After the log-Gabor filtering, the CWT-based peak detection is applied to the filtered radargram. Firstly, a set of wavelet scales (1–15) is applied to detect the peaks to examine which scale is proper for peak detection for SHARAD radargrams over this study site. Fig. 7 shows peak detection results along columns 22, 60, and 160 of the subset radargram shown in the white rectangle in Fig. 3(a). From Fig. 7(a–c), we can see that the high amplitude peaks represent prominent layers or wide peaks. The high wavelet coefficients may result from a sequence of layers rather than a specific layer. Fig. 7(d–f) show the peak numbers detected at each scale from 1 to 15, which indicates that the informative scales are limited within the scale of about 13. Therefore, a scale of 13 is chosen as a limit of the wavelet scale and the Mexican Hat function is selected as the wavelet in the CWT transform over this study site.

By applying this CWT-peak detection to all columns of the radargram, the subsurface reflections can be detected and laid over the original radargrams. Fig. 8 shows two sets of extracted subsurface reflections from SHARAD radargrams for orbits 2202 and 6651. The white dots in Fig. 8(a) and (c) show the detected peaks when using the scales from 1 to 13 while the black dots represent the extracted peaks when using the single scale of 13. When using a single scale of 13, only the prominent reflections are detected while faint reflections are detected when smaller scales are included. To figure out the primary subsurface structures, the single scale 13 is set to extract subsurface reflections for an initial reconstruction though in some areas the detected reflections are not as dense as those detected with the scale range of 1–13. The detected subsurface reflections before and after removal of clutter reflections can be seen in Fig. 8(b) and (d).

4.4. The 3-D processing

After all the subsurface reflections are detected, they are aggregated into a point cloud. Firstly, the DBSCAN algorithm is applied to the point cloud to classify the points based on their density distribution, and to remove noisy points which are distributed with a low density between the clustered groups. After the DBSCAN clustering, all the points are classified into 138 groups, among which there are seven groups containing point numbers of more than 1000. In the next step, a hierarchical clustering is applied to the classified groups to further divide the centroid of the pre-classified 138 groups given the number of primary clusters which is selected as seven in this case. The final partitioned result of this point cloud is shown in Fig. 9.

Each cluster of the points are samples from a subsurface DTM, which can be derived by interpolating the points in this cluster. A Triangulated Irregular Network (TIN) is used in this study to interpolate the points into a subsurface DTM. The interpolated surface (S) and subsurface (SS1-6) DTMs are shown in Fig. 10. These DTMs are provided as supplementary files with a MATLAB code to show them in a 3-D rendering. The subsurface DTMs are then converted to depth maps and shown along with the surface DTM in Fig. 11. Fig. 11(d) displays a depth map of the regional discontinuity (named here as AUR1) which is converted from the AUR1 DTM produced by Guallini et al. (2018). According their study, the AUR1 should correspond to the SS2 shown in Fig. 11(c). Compared to the AUR1, the SS2 depth map shows more detailed variation which may due to the difference in interpolation methods between Kriging and TIN interpolation. This difference can be also caused by less radargrams used for interpolating the AUR1 although more than 600 SHARAD radargrams are inspected in the Promethei Lingula region, which is larger than the AUR1 extent according to Guallini et al. (2018). Besides, the AUR1 DTM is derived not only by subtracting depth from MOLA DTM, but also by further subtracting the average elevation in each SHARAD orbit. Since the AUR1 DTM has already been interpolated, it is hard to take this into account in the depth conversion. Therefore, we add back an offset of 6000 m to the AUR1 DTM. The difference between depth maps of SS2 and AUR1 can also be caused by the fact that the latter is derived by subtracting the average elevation in each orbit rather than each footprint.

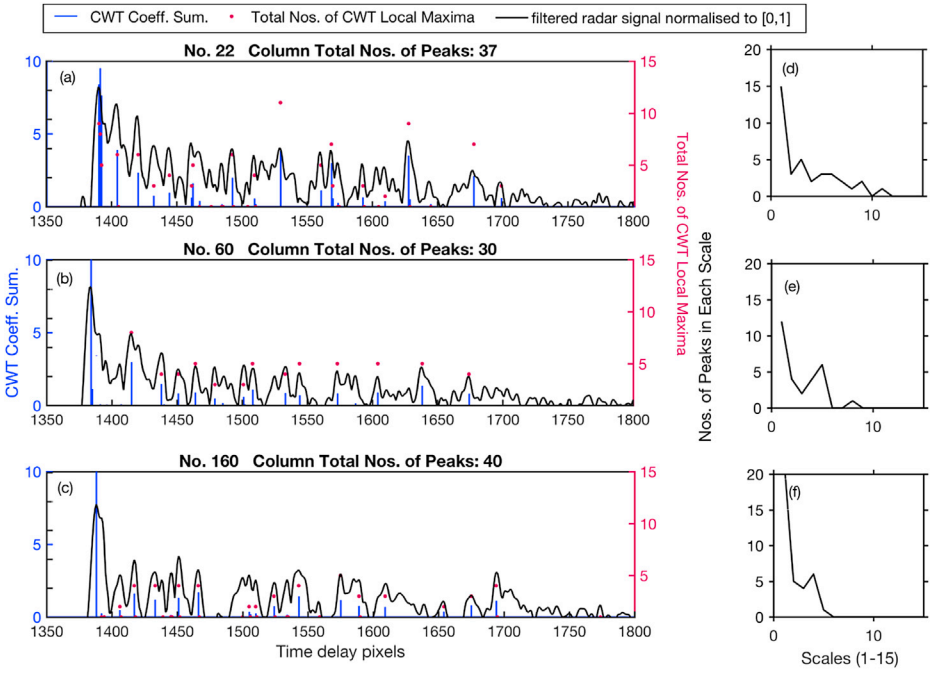

Fig. 7. The CWT-based peak detection of SHARAD data from orbit 2202.

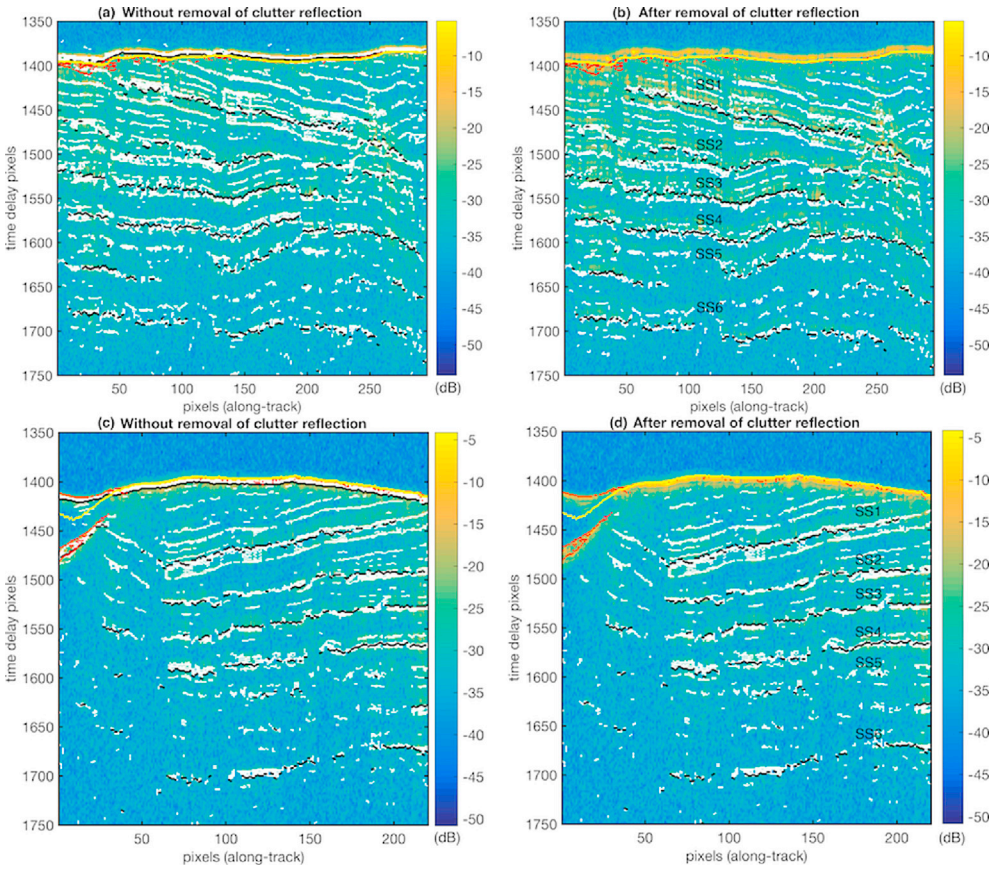

Fig. 8. Subsurface reflections detected by applying CWT-based peak detection method with a single scale of 13 (black dots) and a scale range of 1–13 (white dots), to radargrams from (a) orbit 2202 and (c) orbit 6651; Subsurface reflections after removal of clutter reflections (red dots) (b) for radargram from orbit 2202 and (d) for the radargram from orbit 6651. The yellow lines are the nadir surface and the background image is the original radargrams. (For interpretation of the references to colour in this figure legend, the reader is referred to the Web version of this article.)

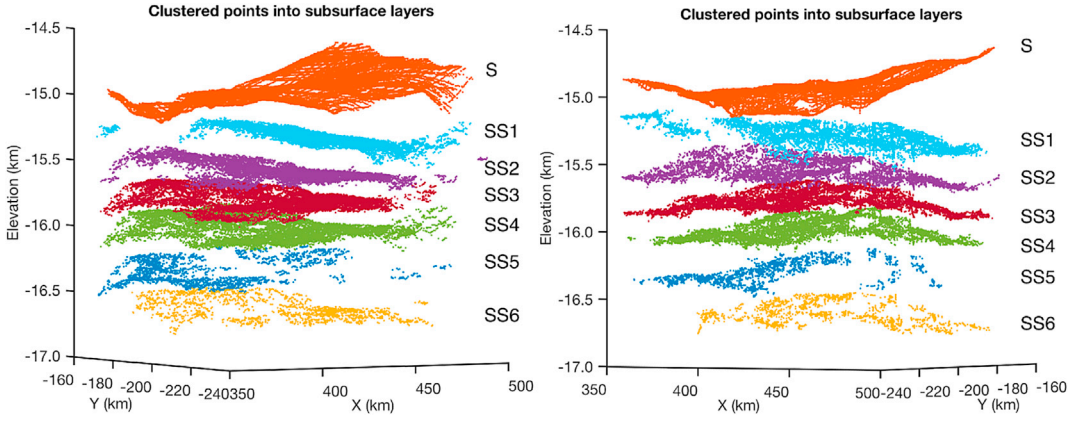

Fig. 9. The clustered 3-D points viewed from azimuth angles of (a) −45° and (b) +45°.

5. Discussion

This study developed an automated workflow to reconstruct subsurface elevation models from SHARAD radargrams and external DTMs, such as HRSC and MOLA DTMs. The primary and prominent subsurface reflections are detected by applying a CWT-based peak detection to the SHARAD radargrams and the removal of clutter reflections is achieved by simulation using the external HRSC DTM. By applying clustering algorithms to the extracted points, the subsurface topography can be reconstructed successfully. Although there is some adjustment of the input parameters to the workflow, the proposed workflow and corresponding tools are easily tuned to different applications and are much faster compared to the manual delineation of subsurface layers. Depending on how many layers there are in the study area, several key parameters, such as the wavelet scale and the distance and sample points used within the DBSCAN clustering, need to be tuned for each area, which usually takes several iterative trials with each trial usually taking a few minutes to achieve.

The CWT-based peak detection is effective in picking strong reflections when selecting a wavelet scale of 13 in this case. However, when the scale is selected as a smaller value, more points from subtle layers can be extracted. By choosing a scale of 13, only the prominent reflections are extracted, which represent the high responses to the wavelet by a layer sequence composed of parallel layers. Therefore, the six subsurface DTMs obtained in this study can be regarded as representations of layer sequences. The removal of clutter reflections works robustly on the strong clutters near the surface. Deeper and weaker clutters bend the layers and this effect is hard to disentangle from the

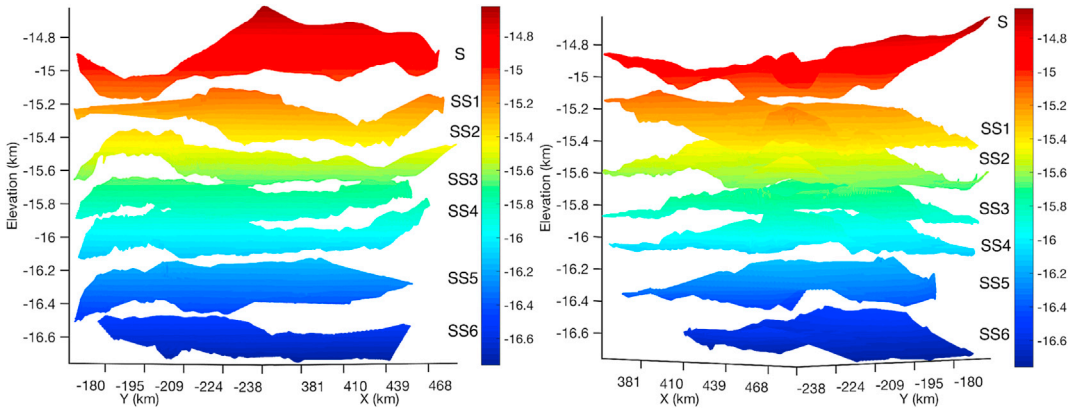

Fig. 10. The interpolated surface and subsurface DTMs which are viewed from azimuth angle of (a) −45° and (b) +45°.

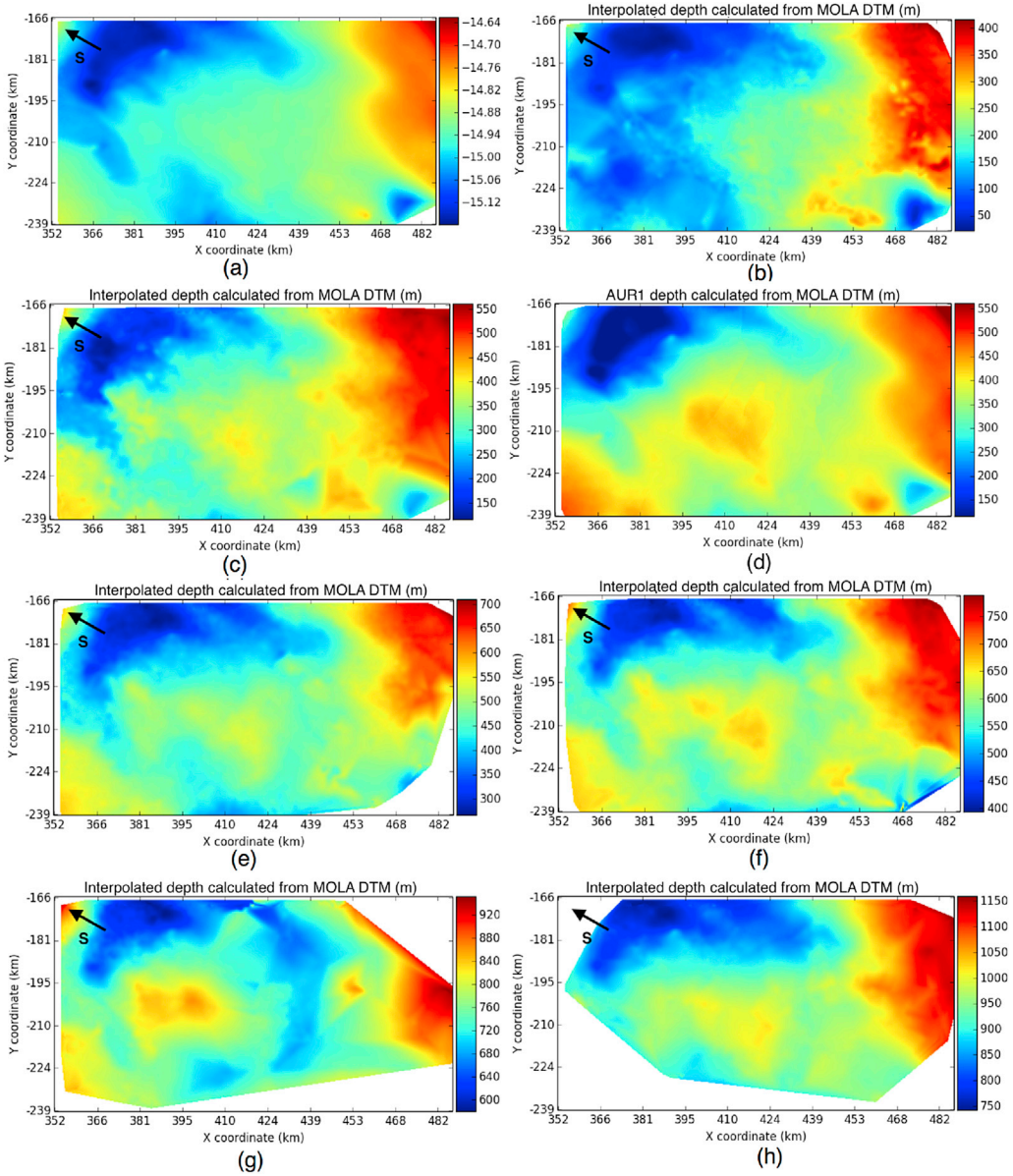

Fig. 11. (A) Interpolated surface DTM; (b–c) and (e–h) are six interpolated subsurface depth maps (SS1-SS6) that are calculated from surface DTM; (d) showing the interpolated AUR1 depth map, in comparison with (c) the depth map of SS2.

layering phenomenon itself. Since the removal of clutter reflections is now simply dependent on the threshold that is related to the intensity of surface returns, the subsurface clutter reflections are not able to be removed in some cases. However, the subsequent DBSCAN clustering can largely remove the sparse distributed reflections including parts of the remaining clutter reflections. DBSCAN is useful to separate the point cloud into several primary groups, while the following hierarchical clustering mainly utilises the information of elevation to separate into different planes, however, the mere dependence on the elevation might lead to bad performance when the subsurface topography has dramatic variations. More advanced and intelligent methods for separating the point clouds into curved layers are needed in the future. The TIN interpolation is currently applied directly to all points which are sometimes very sparsely distributed, so it does not work very well in areas with only very few or even no sample points, such as the northwest part of SS1 and the eastern part of SS5. This issue needs to be addressed in future work.

Compared to the three layer sequences reported in the literature (Kolb and Tanaka, 2006; Milkovich et al., 2009; Guallini et al., 2018), this study reveals six subsurface depth maps (SS1-6) of the Promethei Lingula region, which may indicate detailed depositional and erosional processes. In this region, the subsurface layers are extending into the Chasma Australe while they gradually disappear to the south and north of this chasma towards which the top layer sequences become thicker and thicker. The second layer below the surface (SS2) as shown in Fig. 11(c) corresponds to the AUR1 (Figure 11(d)) produced by Guallini et al. (2018). Although generated by different methods, they share a similar depth variation across this region. Fig. 11(c) and (d) show the same increasing depth away from the south pole in the southern region of the study site. In addition, more details can be observed in the SS2 depth map. The two lower subsurface depth maps (SS3 and SS4) are generally parallel to each other, whilst preserving subtle differences in depth variation as seen in Fig. 11(e and f). Further below is the SS5, which has more sample points in the south of the study site while the sample points are very sparse in the north region. Therefore, the interpolated depth of the region with x coordinates larger than 424 km in Fig. 11(g) is probably not very reliable. Observing the left part ($x < 424$ km) of SS5, a trend of decreasing depth can be observed from the southeast to the northwest of this study area, indicating a convergence with the upper layers to some point in the northwest region. Although the SS5 is not very well reconstructed, the subsurface interface below it (SS6) is reconstructed successfully, which generally follows the depth variation of the SS3 and SS4. It indicates that the detection of SS5 is not out of the capability of the SHARAD instrument, however, it is the subsurface of SS5 vanishing or joining to the upper one at some point that leads to the failure of proper reconstruction.

6. Conclusions

A radar sounding technique has been applied to studying the Martian subsurface for more than a decade. The utilisation of this radar sounding data has been transformed from manual interpretation to automatic processing although many geologic studies still prefer to employ manual delineation. This study proposes an innovative method for automatically reconstructing subsurface DTMs of Martian polar region. Taking the Promethei Lingula region in Martian south pole as an example, the study shows a processing workflow, by which the surface DTM and six subsurface interfaces are reconstructed automatically and successfully.

One of the reconstructed subsurface interfaces correlates with the angular unconformity revealed in previous studies. In addition, this study firstly reveals another subsurface interface (SS5) which tends to converge into the upper layer sequence. It is the first time that a detailed subsurface stratigraphy is reconstructed by an automated workflow. The proposed method and workflow are realised by using Python and developed as a QGIS plugin (SHARAD3d) which is publically available on GitHub (https://github.com/xiongsiting/SHARAD3d) to the scientific community at the time of publication. More areas will be tested in the future with the SHARAD data.

Acknowledgements

The SHARAD dataset is from the Derived Data Products produced by the SHARAD U.S. Science Team and can be downloaded from http://pds-geosciences.wustl.edu/missions/mro/sharad.htm. This work is jointly funded by the China Scholarship Council and University College London by providing a scholarship of Dean of MAPS prize to the first author. The authors would like to thank the ESA-NRSCC DRAGON for their travel support to present preliminary results and the travel support from the European Union's Seventh Framework Programme (FP7/20072013) under iMars grant agreement no 607379 and partial funding was obtained from the STFC "MSSL Consolidated Grant" ST/K000977/1. The authors would like to thank Luca Guallini and Lucia Marinangeli for kindly providing the AUR1 DTM for comparison in this study and to Kiky Putri for kindly providing the corresponding HRSC DTM which is described in Putri et al. (under review).

Appendix A. Supplementary data

Supplementary data related to this article can be found at https://doi.org/10.1016/j.pss.2018.08.001.

References

Al-Nuaimy, W., Lu, H.H., Shihab, S., Eriksen, A., 2001. Automatic mapping of linear structures in 3-dimensional space from ground-penetrating radar data. In: 2001 IEEE/ISPRS Joint Workshop Remote Sensing and Data Fusion over Urban Areas. IEEE, pp. 198–201.

Byrne, S., Ivanov, A., 2004. Internal structure of the Martian south polar layered deposits. J. Geophys. Res. Plan 109. https://doi.org/10.1029/2004JE002267.

Capineri, L., Grande, P., Temple, J., 1998. Advanced image-processing technique for real-time interpretation of ground-penetrating radar images. Int. J. Imag. Syst. Technol. 9, 51–59. https://doi.org/10.1002/(SICI)1098-1098(1998)9:1<51::AID-IMA7>3.0.CO;2-Q.

Chen, G., Qian, S.E., 2011. Denoising of hyperspectral imagery using principal component analysis and wavelet shrinkage. IEEE Trans. Geosci. Rem. Sens. 49, 973–980. https://doi.org/10.1109/TGRS.2010.2075937.

Dabov, K., Foi, A., Katkovnik, V., Egiazarian, K., 2007. Image denoising by sparse 3-d transform-domain collaborative filtering. IEEE Trans. Image Process. 16, 2080–2095. https://doi.org/10.1109/TIP.2007.901238.

Delbo, S., Gamba, P., Roccato, D., 2000. A fuzzy shell clustering approach to recognize hyperbolic signatures in subsurface radar images. IEEE Trans. Geosci. Rem. Sens. 38, 1447–1451. https://doi.org/10.1109/36.843039.

Du, P., Kibbe, W.A., Lin, S.M., 2006. Improved peak detection in mass spectrum by incorporating continuous wavelet transform-based pattern matching. Bioinformatics 22, 2059–2065. https://doi.org/10.1093/bioinformatics/btl355.

Ester, M., Kriegel, H.P., Sander, J., Xu, X., 1996. A density-based algorithm for discovering clusters in large spatial databases with noise. In: The Second International Conference on Knowledge Discovery and Data Mining, pp. 226–231.

Ferro, A., Bruzzone, L., 2013. Automatic extraction and analysis of ice layering in radar sounder data. IEEE Trans. Geosci. Rem. Sens. 51, 1622–1634. https://doi.org/10.1109/TGRS.2012.2206078.

Flamini, E., Fois, F., Calabrese, D., Bombaci, O., Catallo, C., Croce, A., Croci, R., Guelfi, M., Zampolini, E., Picardi, G., Seu, R., Mecozzi, R., Biccari, D., Cartacci, M., Cicchetti, A., Masdea, A., Alberti, G., Maffei, S., Papa, C., 2007. Sounding Mars with SHARAD & MARSIS. In: 2007 4th International Workshop on Advanced Ground Penetrating Radar. IEEE, pp. 246–251. https://doi.org/10.1109/AGPR.2007.386561.

Foss, F.J., Putzig, N.E., Campbell, B.A., Phillips, R.J., 2017. 3D imaging of Mars' polar ice caps using orbital radar data. Lead. Edge 36, 43–57. https://doi.org/10.1190/tle36010043.1.

Freeman, G.J., Bovik, A.C., Holt, J.W., 2010. Automated detection of near surface Martian ice layers in orbital radar data. In: 2010 IEEE Southwest Symposium on Image Analysis & Interpretation (SSIAI). IEEE, pp. 117–120. https://doi.org/10.1109/SSIAI.2010.5483905.

Gamba, P., Lossani, S., 2000. Neural detection of pipe signatures in ground penetrating radar images. IEEE Trans. Geosci. Rem. Sens. 38, 790–797. https://doi.org/10.1109/36.842008.

Guallini, L., Rossi, A.P., Forget, F., Marinangeli, L., Lauro, S.E., Pettinelli, E., Seu, R., Thomas, N., 2018. Regional stratigraphy of the south polar layered deposits (Promethei Lingula, Mars): "Discontinuity-bounded" units in images and radargrams. Icarus 308, 76–107. https://doi.org/10.1016/icarus.2017.08.030.

Kim, J.R., Muller, J.P., 2009. Multi-resolution topographic data extraction from Martian stereo imagery. Planet. Space Sci. 57, 2095–2112. https://doi.org/10.1016/j.pss.2009.09.024.

Kolb, E.J., Tanaka, K.L., 2006. Accumulation and erosion of south polar layered deposits in the Promethei Lingula region, Planum Australe, Mars. Int. J. Mars Sci. Explor. 2, 1–9. https://doi.org/10.1555/mars.2006.0001.

Kovesi, P., 1999. Phase preserving denoising of images. Signals 4.

Milkovich, S., Plaut, J., Safaeinili, A., Picardi, G., Seu, R., Phillips, R., 2009. Stratigraphy of Promethei Lingula, south polar layered deposits, Mars, in radar and imaging data sets. J. Geophys. Res. Plan 114. https://doi.org/10.1029/2008JE003162.

Mouginot, J., Pommerol, A., Kofman, W., Beck, P., Schmitt, B., Herique, A., Grima, C., Safaeinili, A., Plaut, J., 2010. The 3–5 MHz global reflectivity map of Mars by MARSIS/Mars Express: implications for the current inventory of subsurface H2O. Icarus 210, 612–625. https://doi.org/10.1016/j.icarus.2010.07.003.

Papari, G., Petkov, N., 2011. Edge and line oriented contour detection: state of the art. Image Vis Comput. 29, 79–103. https://doi.org/10.1016/j.imavis.2010.08.009.

Pasolli, E., Melgani, F., Donelli, M., 2009. Automatic analysis of GPR images: a pattern-recognition approach. IEEE Trans. Geosci. Rem. Sens. 47, 2206–2217. https://doi.org/10.1109/TGRS.2009.2012701.

Putri, A.R.D., Sidiropoulos, P., Muller, J.P., Walter, S., Michael, G.G., A New South Polar Digital Terrain Model of mars from the High Resolution Stereo Camera (HRSC) Onboard the ESA Mars Express for Tracking Changes over the SPRS, Planet. Space Sci. (Under review).

Seu, R., Biccari, D., Orosei, R., Lorenzoni, L., Phillips, R., Marinangeli, L., Picardi, G., Masdea, A., Zampolini, E., 2004. SHARAD: the MRO 2005 shallow radar. Planet. Space Sci. 52, 157–166. https://doi.org/10.1016/j.pss.2003.08.024.

Seu, R., Phillips, R.J., Alberti, G., Biccari, D., Bonaventura, F., Bortone, M., Calabrese, D., Campbell, B.A., Cartacci, M., Carter, L.M., et al., 2007. Accumulation and erosion of Mars' south polar layered deposits. Science 317, 1715–1718. https://doi.org/10.1126/science.1144120.

Steger, C., 1996. Extracting curvilinear structures: a differential geometric approach. In: European Conference on Computer Vision. Springer, pp. 630–641. https://doi.org/10.1007/BFb0015573.

Tomasi, C., Manduchi, R., 1998. Bilateral filtering for gray and color images. In: Sixth International Conference on Computer Vision, 1998. IEEE, pp. 839–846. https://doi.org/10.1109/ICCV.1998.710815.

Torrence, C., Compo, G.P., 1998. A practical guide to wavelet analysis. Bull. Am. Meteorol. Soc. 79, 61–78. https://doi.org/10.1175/1520-0477(1998)079<0061:APGTWA>2.0.CO;2.

Vaughan, D.G., Corr, H.F., Doake, C.S., Waddington, E.D., 1999. Distortion of isochronous layers in ice revealed by ground-penetrating radar. Nature 398, 323. https://doi.org/10.1038/18653.

Waddington, E.D., Neumann, T.A., Koutnik, M.R., Marshall, H.P., Morse, D.L., 2007. Inference of accumulation-rate patterns from deep layers in glaciers and ice sheets. J. Glaciol. 53, 694–712. https://doi.org/10.3189/002214307784409351.

Xiong, S., Muller, J.P., Carretero, R.C., 2017. A new method for automatically tracing englacial layers from MCoRDS data in NW Greenland. Rem. Sens. 10, 43. https://doi.org/10.3390/rs10010043.